Chemical
Science

ROYAL SOCIETY
OF CHEMISTRY

PERSPECTIVE

View Article Online
View Journal | View Issue

Check for updates

Cite this: *Chem. Sci.*, 2021, **12**, 517

All publication charges for this article have been paid for by the Royal Society of Chemistry

Received 26th November 2020
Accepted 16th December 2020

DOI: 10.1039/d0sc06496c

rsc.li/chemical-science

Interstitial and substitutional light elements in transition metals for heterogeneous catalysis

Tianyi Chen, Christopher Foo and Shik Chi Edman Tsang *

The addition of foreign element dopants to monometallic nanoparticle catalysts is of great importance in industrial applications. Both substitutional and interstitial doping of pure metallic phases can give profound effects such as altering electronic and transport properties, lattice parameters, phase transitions, and consequently various physicochemical properties. For transition metal catalysts, this often leads to changes in catalytic activity and selectivity. This article provides an overview of the recent developments regarding the catalytic properties and characterisation of such systems. In particular, the structure–activity relationship for a number of important chemical reactions is summarised and the future prospects of this area are also explored.

Introduction

Transition metals are often used in heterogeneous catalysis because of their characteristic unfilled d-bands.[1] It has been long known that their catalytic performance can be altered by adding impurities, either deliberately or otherwise. The resulting doping can be broadly classified into substitutional doping[2] and interstitial doping.[3] In substitutional doping, atoms of the host metal are replaced by foreign atoms (Fig. 1a); meanwhile in interstitial doping, foreign atoms, usually light elements, occupy the interstitial sites (Fig. 1b).

The history of interstitial light-element modification of transition metals for catalysts can be dated back to the modification of tungsten by alloying with carbon atoms forming tungsten carbide, which was used in the isomerisation of neopentane to isopentane,[4] and displayed a similar catalytic behavior to platinum metal. Some kinds of geometric and electronic modifications of the host structure by the carbon 'impurities' critically affect surface and/or bulk structure to give significant improvement in catalytic conversion and selectivity.[5] However, despite the dramatic alteration of the catalytic properties by such light-element doping, there is a lack of in-depth understanding of the structure–activity relationship. Recent advances in analytical techniques such as electron ptychography in transmission electron microscopy, and high-resolution

---

Wolfson Catalysis Centre, Department of Chemistry, University of Oxford, Oxford OX1 3QR, UK. E-mail: edman.tsang@chem.ox.ac.uk

Tianyi Chen obtained her BSc (Chemistry) and MRes (Catalysis: Chemistry and Engineering) from Imperial College London (UK) in 2015 and 2016, respectively. In 2020, she completed her PhD thesis at the University of Oxford (UK), under the supervision of Prof. Edman Tsang and Prof. Peter Nellist. Her interests include synthesis and characterisation of light elements doped transition metals and their use as catalysts in the conversion of biomass-derived substrates to value-added chemicals.

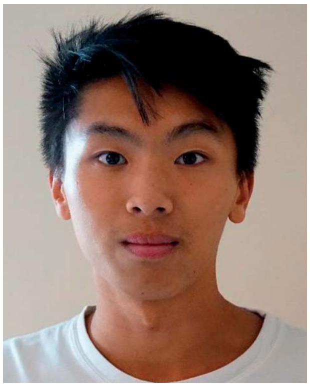

Christopher Foo obtained his MSci degree from the University of Bristol in 2017, and is now a DPhil candidate at the University of Oxford, UK under the supervision of Prof. Edman Tsang. His current research focuses on the crystallographic characterisation of various catalysis and energy storage systems, in particular the identification and siting of dopants in parent frameworks, ranging from zeolites and protonic conductors to lithium ion intercalation for battery applications. Being partly funded and supervised by the nearby Diamond Light Source, he specialises in the collection and refinement of high quality diffraction data in order to correlate emergent properties with atomic structure.

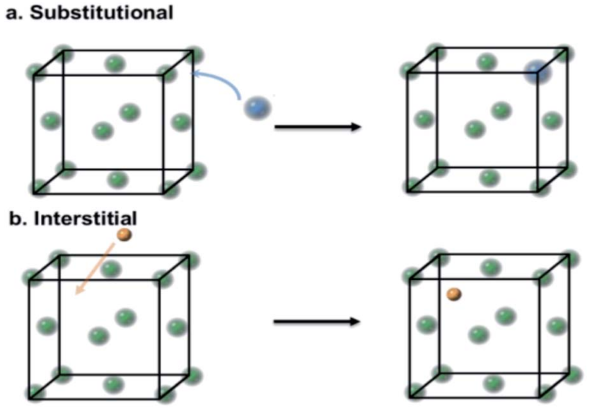

Fig. 1 A schematic of substitutional and interstitial atomic modification by light elements to face-centered-cubic (FCC) a host metal lattice (green). (a) Substitutional atomic displacement by foreign light atoms (blue). (b) Interstitial atomic modification by foreign light atoms (brown).

synchrotron and neutron diffraction have made strong contributions to the understanding of these catalysts, and consequently the correlations between doping, structure and activity, allowing the rational design of this class of catalysts.[6] It is timely to summarise some recent breakthroughs in this area.

Here, in this mini-review, we will outline some of the latest developments in this type of doped transition-metal catalysts, which have been modified with light elements, including hydrogen (H), lithium (Li), boron (B), carbon (C), and nitrogen (N). To provide a more comprehensive understanding, we will also highlight some recent advances in their characterisation with respect to (1) structural aspects: phase identification, local disorder, chemical environment and site location identification; (2) electronic modifications of local and band structure of the host transition metal by DFT calculations; (3) identification and disentanglement of the effects of structural and electronic changes on the observed catalysis phenomena, and give a rational guidance on how modifications of the fundamental physicochemical properties affect catalytic properties; and finally (4) the evaluation of future prospects on the current research field and suggestion of challenges to be overcome.

Edman Tsang is a Professor of Chemistry and Head of Wolfson Catalysis Centre at the University of Oxford, UK. His main research interests are on nanomaterials and catalysis concerning energy and environment which include developments of catalytic, photocatalytic and electrocatalytic technologies for fine chemicals, cleaner combustion, green chemistry, energy storages, processes and production, etc. Particular expertise is in design and architecture of nanocatalysts, which can lead to understanding of catalytic surfaces and interfaces. He has about 350 referred research publications including Nature, Science and Nature sister journals. He has delivered over 200 plenary and invited presentations at conferences, universities and companies.

Terminology: intermetallic compounds *versus* solid-solution alloys and doping

It is well known that the architecture of the nanocrystal, after alloying with foreign atoms or additives, are modified in terms of crystallinity and disorder, local atomic arrangement and symmetry (space group), various types of structural or electronic defects, long/short-range atomic order and distribution, crystal morphology, and secondary architecture properties including sintering/agglomeration behaviour and support distribution.

Regarding the atomic ordering, mixed nano-alloys can further be categorised as either intermetallic compounds or solid-solution alloys (Fig. 2).[7] The term 'intermetallic compound' is used for systems that have long-range atomic order and well-defined stoichiometry. The space group and atomic arrangements of the intermetallic phase are different to that of the pure parent metal. In contrast, the term 'solid-solution alloy' is used to describe a system of two or more components in which the atomic structure of the parent metal is largely unchanged and the dopant is accommodated non-stoichiometrically and distributed non-homogeneously (mixed), *i.e.* the dopant is dissolved in an unchanged structure. This type of doping is usually characterised by gradual changes in lattice parameter with dopant concentration,[8] and may precede a discrete phase transition to an intermetallic compound,[9] which can be demonstrated by the boron–palladium binary system.[8,9]

The formation of solid-solution alloys or intermetallic compounds can be explained from a thermodynamic perspective (eqn (1)):[10]

$$\Delta G_\mathrm{f} = \Delta H_\mathrm{f} - T\Delta S_\mathrm{f} \tag{1}$$

where ΔH_f and ΔS_f are the formation enthalpy and entropy, respectively, for alloying from the pure metal; T is the absolute temperature. When the properties of the constituent elements are very close, ΔH_f is close to zero or slightly negative. Therefore,

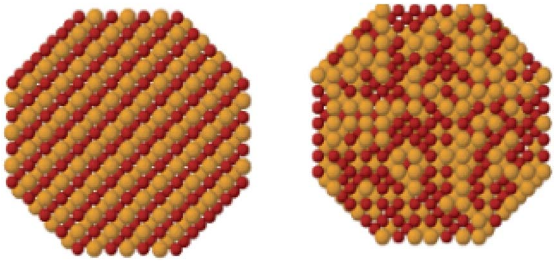

Fig. 2 A schematic representation of intermetallic compounds (left) and solid-solution alloys (right). This figure has been reproduced from ref. 12 with permission from American Chemical Society, copyright 2008.

the disordered structure ($\Delta S_f > 0$) is favourable, and hence a negative ΔG_f is obtained, but the ordered structure cannot be explained in terms of entropy. Nevertheless, if the electronic properties of the constituent elements are very different, a highly negative ΔH_f is sufficient to compensate for the entropy loss, leading to a negative ΔG_f. However, in the case where the elements have similar properties, the doped structures can form both ordered and disordered structures, resulting in intermediate properties between the behaviour of intermetallic compounds and solid-solution alloys. Ordered alloys are called Kurnakov-type intermetallic compounds, and their transition to disordered structures can be driven by enhancing the contribution of $-T\Delta S_f$.[11]

Therefore, the driving force in the formation of solid-solution alloys (entropy-driven) and intermetallic compounds (enthalpy-driven) are different. However, it is worth noting that this equation fails to consider the factors of strain, defects *etc.*[10] Overall, this classification is essential because solid-solution alloys and interatomic compounds behave differently even if the elemental composition and stoichiometry are the same.

In literature, the term 'doping' is used most frequently to describe the addition of a small quantities of a foreign element as a promoter or additive to a catalyst or semiconductor. This type of 'doping' is usually described in a general, non-specific way. In this work, this term will also be used to describe large concentrations of additive; for example in Y-doped ZrO_2, in which the Y content is above 10%. As admitted by the literature,[13] as long as the modification is mild and the parent structure remains approximately unchanged, this term is still applicable. Therefore, it is more suitable to use the term 'doping' when describing solid-solution alloys and use other words when describing intermetallic compounds.

Solid-solution alloy: substitutional *versus* interstitial systems

Substitution systems

For typical substitutional solid-solution alloys, the atomic size and electronic properties of the foreign element are similar or identical to that of the parent metal. Normally, the difference in atomic radius should be less than 15%, as described by the Hume–Rothery rule[14] (eqn (2)).

$$\left(\frac{r_{\text{solute}} - r_{\text{solvent}}}{r_{\text{solvent}}}\right) \times 100\% \leq 15\% \qquad (2)$$

The formation of substitutional alloys can affect the local electronic structure, thereby modifying the chemisorption properties of the metal surface.[15] This occurs in both zero valent and metal oxide systems. For example, Cu can be alloyed into Ni, leading to the formation of a substitutional alloy.[16] The presence of Cu in the substitutional alloy system is anticipated to fill the d-band vacancies of Ni and suppress the formation of γ-NiOOH, which is a low-activity byproduct formed during electrocatalytic methanol oxidation. In the case of substitutional alloy formation in metal oxides, a small fraction of the metal cations of a host oxide can be substituted by foreign cations,[17] and/or the anions replaced by foreign anions such as halides.[18] Though, as known in the literature, the stability of substitutional alloys is a problem because the dopant atom often does not have strong location preference with a low mobility barrier resulting in diffusion and instability at elevated temperatures. Hence, segregation or even loss of dopant can occur, resulting in a mixture of the pure constituents.[19]

Interstitial systems

Unlike substitutional alloys, in order for the formation of interstitial alloys to occur, the size of the foreign species needs to be sufficiently small to diffuse into the interstitial sites. The conventional interstitial alloys are metal hydrides,[20] carbides,[21] borides[22] and nitrides,[23] among others. These light elements, from the first period of the p-block and below, often have small atomic radii and dominant s–p orbitals, and often occupy the largest available interstitial site: the octahedral hole in face-centre-cubic (FCC) and hexagonal-close-packed (HCP) structures, and the trigonal prismatic hole in hexagonal structures. The crystal structure is governed by geometric and electronic factors. The geometric factor is based on Hägg's rule,[24] which uses the ratio of dopant atomic radius (r_X) to that of the host metal atomic radius (r_M) for the interstitial alloy formation. When the ratio (r_X/r_M) is less than 0.59, the structure of the interstitial alloy will be simple, such as the aforementioned FCC, HCP and hexagonal structures. When the ratio (r_X/r_M) is greater than 0.59, an interstitial alloy with a more complicated structure will be obtained, for instance chromium carbide, Cr_3C_2.[25]

The second factor that governs crystal structure is the electronic effect. The nature of metallic bonding in interstitial solid-solution transition-metal alloys (d-orbital dominated) is remarkably different to the pristine metal due to orbital mixing between the foreign atoms and host metal system, such as the s–p orbitals of the dopant element and the s–p–d orbitals of the metal elements. In light of the Engel–Brewer theory of metals,[26,27] it was suggested that the structure adopted by a metal or interstitial solid-solution alloy is dependent on the s–p counts as follows:[26]

BCC: $sp^{0.5}$
HCP: $sp^{0.7-1.1}$
FCC: $sp^{1.5-2}$

It can be found that increasing p-orbital mixing can induce the structural transformation from body-centre-cubic (BCC) to HCP to FCC. Additionally, accommodating foreign atoms in a metal structure can result in lattice expansion of the host structure, which is indicative of interstitial solid-solution alloy formation due to repulsive electrostatic interactions.[28]

The size of solute is a main contribution for the formation of the interstitial solid-solution alloy. As depicted in Fig. 3, the atomic radii of hydrogen, boron, carbon and nitrogen are rather small. However, the atomic radius of Li is relatively large, comparable to some transition metals such as silver (165 pm). Hence, lithium atoms are observed to substitute silver atoms instead of inhabiting interstitial sites in the structure.[128] Hence,

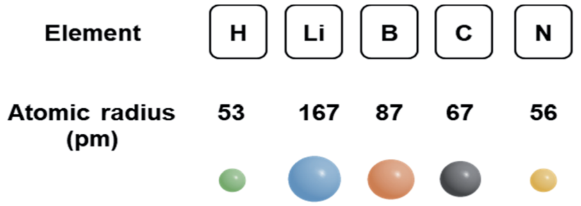

Fig. 3 The atomic radii of elemental hydrogen, lithium, boron, carbon and nitrogen.

it is expected that incorporating light elements with smaller atomic radii into transition metals are more likely to form interstitial solid-solution alloys. In addition to the effect of size, the similarity of the electropositivity and crystal structure of the two components needs to be taken into account when considering interstitial solid-solution systems.[29]

Since each research group has its own notation for solid-solution alloy systems, this mini-review will express binary systems with the host metal (M) first, and the dopant element (N) second. Substitutional doping and interstitial doping will be expressed in superscript as follows: M–$^{\text{sub}}$N and M–$^{\text{int}}$N. Solid-solution phases that are reported as a specified composition are expressed as M_mN_n. Unclear solid-solution phases are expressed as M_mN_x, where x denotes that the atomic ratio remains unclear. In bimetallic systems that have been doped with a light element, the two host metals will be separated by a dash. Note that some material labels in this mini-review differ from the original ones in the literature.

Characterisation

As emphasised, once the foreign element either substitutes an atom from the metal framework or occupies an interstitial site, even at very low concentration, profound effects on the physiochemical properties of the host metal system can be altered, such as adjusting the electronic and transport properties, lattice parameter changes, phase transitions, thermal stability and chemical properties, *etc.* However, regardless of synthetic method used, it is difficult to discern whether the foreign element has been deposited on the surface, at interstitial sites or vertices of the host metal system. Therefore, if the catalytic performance is promoted after addition of the foreign additives, it is anticipated that confirming the location and the degree of occupancy of the foreign elements will significantly contribute to the understanding of the relationship between the dopant-host metal system and catalytic performance.

As reflected from literature,[17] the employment of appropriate characterisation techniques can help answer these questions:

What drives the accommodation?

What is the chemical state/properties of the foreign elements?

What sites do the foreign elements occupy?

Is the resulting structure crystalline, or only ordered at a short length-scale?

Is the foreign element homogeneously distributed throughout a particle, *i.e.* surface/bulk distribution?

Can we visualise the dopants directly?

Following advances in the sensitivity of detection and the speed of digital processing, many more state-of-the-art techniques for characterisation have been developed (Table 1). In the following section, the methods used to help answering the above questions will be evaluated.

X-ray diffraction (XRD)

The accommodation of light elements induces structural distortion of the host metal system, for example the presence of carbon in the interstitial site of palladium.[39] Normally, the diffraction patterns of the modified system are compared with that of the unmodified system to observe whether the reflections are shifted or new phases are formed. It should be noted that not every case will obey this rule. In recent work on the Au–$^{\text{int}}$C system, doping does not induce any appreciable change in diffraction.[40] Expansion or contraction due to substitutional modification is usually interpreted using Vegard's rule,[17] which states that the concentration of a substitutional dopant is linearly correlated with the variation in the lattice parameter. However, it should be noted that Vegard's rule does not have a sound theoretical basis, as is often admitted by literature, with many exceptions reported.[41]

Compared to laboratory-source X-rays, those from a synchrotron source have many improved properties, for example brightness, focus area, divergence, and energy bandwidth. Additionally, much higher energies can be achieved. Highly collimated and intense X-rays allow the collection of high-resolution X-ray data, particularly for diffraction. For example, in our recent work, the refinement of high-resolution synchrotron X-ray powder diffraction (SXRD or SXPD) patterns demonstrated the coexistence of FCC and HCP phases in Pd–$^{\text{int}}$B NPs.[6]

Other characterisation by synchrotron radiation

Other experiments carried out at synchrotron-radiation facilities include the following. Use of the X-ray pair distribution function (XPDF) and the corresponding refinement can probe the local structure, distortion and site occupancy for disordered systems.[6] Also useful in characterising non-crystalline systems, extended X-ray absorption fine structure (EXAFS) and X-ray absorption near-edge structure (XANES) can determine the chemical composition, electronic state, environment and local structure, regardless of long-range order.[31] For example, the use of XANES spectra is capable of detecting the Pd–C bonds of carbon-containing molecules adsorbed at the surface of Pd NPs. In studies of the Pd–$^{\text{int}}$H phase, Lamberti *et al.*[42] used *in situ* and *in operando* X-ray absorption spectroscopy (XAS) to demonstrate the differences in structural and electronic configuration between the core and shell regions of the NP, due to hydriding at different temperatures and hydrogen pressures.

X-ray photoelectron spectroscopy (XPS)

XPS is a conventional technique that is used to probe the surface composition and chemical state of solid catalysts, due to the very low penetration depth of the photoelectrons. It is often

Table 1 Analytical techniques used in the characterisation of light-element modification of transition-metal NPs[17]

Incident particle	Analytical technique	Main information	Ref.
Photons	XRD	Atomic positions and occupancies of crystalline structures	30
	EXAFS/XANES	Interatomic distances, chemical environments/oxidation states	31
	XPS	Electronic structure, oxidation states	32
	XPDF	Distorted local structure	6
	FTIR	Vibrational frequency of intermediates on metallic surface	33
Electron	S/TEM	Crystal structure of nanoparticles	34 and 35
	EELS/EDX	Chemical composition/oxidation states	36 and 37
	Ptychography, DPC	Imaging of light elements	38
Other	ssNMR	Chemical environment of light elements	6
	TPR	Oxidation states, oxidative and thermal stability	30
	DSC/TGA	Thermal stability	30
	ICP/MS	Elemental composition	32

used to determine the oxidation states and concentrations of sub/surface atoms, which provides complementary information to XRD. Liu *et al.* synthesised mesoporous Pd–$^{\mathrm{int}}$B nanospheres (MNSs) by using amphiphilic dioctadecyldimethylammonium chloride (DODAC) as the surfactant template, and confirmed the synthesis of the phase by XRD and XPS. Notably, partial electron transfer to the metal framework was observed by the Pd $3d_{5/2}$ binding energy in Pd–$^{\mathrm{int}}$B shifting to significantly higher energy (336.1 eV *vs.* 335.1 eV), which is indicative of partial band filling.

Fourier-transform infrared spectroscopy (FTIR)

FTIR spectroscopy is used to probe the variations in vibrational frequencies of metal–adsorbate bonds. Bowker *et al.*[43] compared the CO absorption on doped and undoped Pd NPs using diffuse-reflectance infrared Fourier-transform spectroscopy (DRIFTS). For the reduced undoped Pd NPs, a band located at ~1990 cm^{-1} was observed when exposed to CO, which was assigned to the bridge-bonded CO on Pd. However, this band of ~1990 cm^{-1} was not seen in the carbidised sample, which indicates that the presence of carbon at the interstitial sites can alter the surface structure and block the bridge site adsorption, alleviating poisoning.

Additionally, FTIR can be used to give insight into the catalytic mechanism under typical reaction conditions. Cai *et al.*[44] studied the decomposition of formic acid over Pd–$^{\mathrm{int}}$B/C and undoped Pd/C. The Pd/C exhibited a distinctive CO band from adsorbed formic acid. In contrast, for the Pd–$^{\mathrm{int}}$B/C, there was negligible signal in the CO region (1800–1900 cm^{-1}), and the predominant band was indicative of adsorbed CO_2. This result indicates the subtle change in the reaction pathway for the formic acid dehydrogenation over Pd when doped with B.

Probing interstitial light elements with electrons

It is well known that electron microscopy can provide structural and morphological information of doped metallic nanoparticles.[45] Benefiting from development in aberration correctors and computational processing, scanning transmission-electron microscope annular dark-field imaging (STEM-ADF) is becoming an important analytical technique to study this class of materials. However, it is rather challenging to directly visualise light elements such as hydrogen, carbon, boron, and nitrogen within the metal lattice due to their low atomic number and hence low electron-scattering ability, which is in stark contrast with highly scattering metal atoms.[46] Furthermore, for light-element dopants, additional care must be taken to avoid beam damage when using intense electron beams. In an investigation of an interstitially boron-doped palladium catalyst, Pd–$^{\mathrm{int}}$B, our research group used the emerging electron microscopy technique of ptychography to visualise boron at the octahedral sites of the Pd metal framework.[6] Along with other supporting techniques and simulations, certain atomic columns observed by microscopy were interpreted as interstitial boron atoms. In 2020, Gan *et al.*[47] reported that the use of a differentiated and integrated differential phase contrast technique (dDPC and iDPC) in aberration-corrected STEM can even directly visualise atomic columns of hydrogen that correspond to interstitial tetrahedral sites in the Pd–H system, which was also supported by the simulated dDPC images. On the basis of the result, they claimed that hydrogen can also occupy tetrahedral interstitial sites, which is in agreement with previous NPD studies[48] and theoretical calculations.[49]

Electron microscopy is often associated with two spectroscopic techniques that yield elemental mapping information. Energy-dispersive X-ray (EDX) spectroscopy can yield elemental composition information, and specialises in the detection of heavy elements. Meanwhile electron energy-loss spectroscopy (EELS) is additionally able to probe the local chemical environment and oxidation state, and specialises in the detection of light elements. Recently, our research group used EELS to map the boron distribution within Pd NPs and estimated the site occupancy of boron at octahedral sites to be approximately 0.2.[6] However, the PDF refinement proposed that the average site occupancy across the whole sample was much lower at ~0.05; hence it was shown that interstitial boron is distributed unevenly across the sample. The dopant was shown to be present as atomic boron within the lattice by the observation of the B K-edge at 188 eV, rather than an energy of 194 eV and 203 eV which is indicative of boron oxides (Fig. 4).[6]

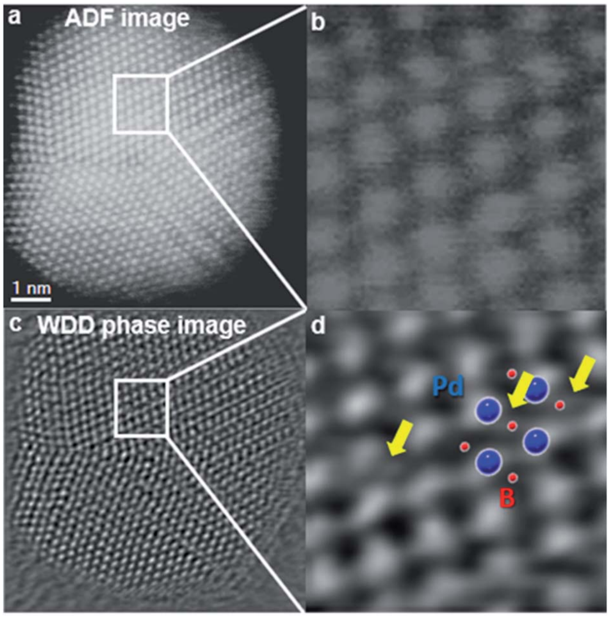

Fig. 4 Simultaneously acquired (a) Z-contrast STEM-ADF (b) inset, and (c) ptychographic phase images of a Pd–^{int}B/C NP oriented in the [110] zone axis. The ptychographic phase image is reconstructed using a Wigner distribution deconvolution (WDD) method after aberration correction. (d) Shows an enlarged area in which some scattering between the Pd columns can be superimposed by the model predicted by XPDF. This figure has been reproduced from ref. 6 with permission from American Chemical Society, copyright 2019.

ICP-MS and ssNMR

Inductively coupled plasma mass spectrometry (ICP-MS) is a powerful analytical technique that can provide elemental composition to ppb sensitivity. For instance, Sato *et al.* quantified the boron composition of Pd–^{int}B NPs synthesised by an electroless deposition method.[50] However, ICP-MS is unable to give information about the location or environment of species. Our research group used ^{11}B magic-angle spinning solid-state NMR (ssNMR) to determine the chemical environment of B in Pd–^{int}B.[6] Deconvolution of the spectra can show the presence of at least two chemical environments, of which one was attributed to the interstitial site and one to surface boron species. Additionally, comparison of the spin-lattice relaxation time T_1 identified which peak corresponded to the interstitial B, as it has a faster relaxation due to its closer proximity to other atoms.

Thermal gravimetric analysis (TGA)

TGA is a conventional analytical technique used to study the stability of interstitially-doped metal catalysts. Takanabe *et al.* used TGA and XANES simultaneously to evaluate the oxidation behaviour of cobalt NPs with and without interstitial boron dopants in CO_2. On the basis of the weight change, the result indicated that the oxidation occurs at a lower temperature in the B-doped system in comparison with the fresh catalyst (boron oxidation on the surface encourages the formation of volatile boron oxide).[51]

Temperature programmed reaction (TPR)

TPR is often used to find the most efficient reduction temperature for catalysts. Additionally, TPR is becoming a quick preliminary method for determining whether a dopant resides at the interstitial sites or not. Owing to the formation of interstitial hydride in palladium at sub-ambient temperatures, our research group showed that if interstitial sites are not blocked by foreign small-elements dopants, TPR yields a strong negative peak at approximately 70–80 °C which is attributed to β-PdH$_x$ decomposition. In contrast, the disappearance of this peak is due to the occupancy of carbon dopants at the interstitial sites.[39]

Computational investigation

Unlike homogeneous catalysis, only surface atoms of close packed heterogeneous catalyst can participate in the chemical reaction. Therefore, is it crucially important to understand how the foreign light elements that occupy interstitial sites alter the surface atomic and electronic structure of a catalyst. In recent decades, computational simulations have become an important tool since they can disentangle complex phenomena and provide information that experiments cannot provide. Hence theoretical simulations are needed for the correlation of structure with chemical properties, which has repeatedly supported experimental testing and characterisation.

Nørskov *et al.* conducted pioneering research into the role of subsurface carbon in palladium during selective hydrogenation by conducting DFT calculations.[52] They identified the absorption energies of carbon at different sites in the Pd metal framework, and showed that the adsorption energy of a methyl group varies as a function of carbon coverage. It was found that the binding of methyl groups is substantially weakened if the carbon resides at the subsurface layer of Pd (111). As indicated, the presence of light elements can expand the unit cell, which can lead to lattice strain. Yang *et al.*[53] compared the electronic effect induced by lattice strain and electronic interaction in the presence of boron atoms during their computational analysis of the hydrogenation of CO to methanol. As demonstrated in

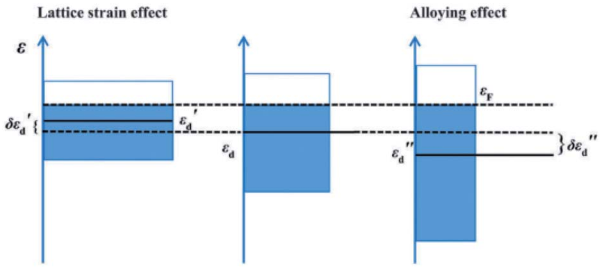

Fig. 5 A schematic illustration of the electronic effect provided by lattice strain (left) and electronic interaction (right) in the presence of boron atoms, compared to pure Pd is (middle). ε_F is the Fermi energy; $\varepsilon_d'(\varepsilon_d'')$ is the energy of the d-band centre and $\delta_{\varepsilon_d'}(\delta_{\varepsilon_d''})$ is the shift of the d-band centre, where $\delta_{\varepsilon d'} = \varepsilon_d' - \varepsilon_d$ and $\delta_{\varepsilon d''} = \varepsilon_d'' - \varepsilon_d$. This figure has been reproduced from ref. 53 with permission from Royal Society of Chemistry, copyright 2016.

Fig. 5, the lattice-strain effect can shift the d-band of palladium to higher energy;[54] ε_d shifts to ε_d' with an increment of ε_d''. Meanwhile the alloying effect can broaden the d-band of palladium. Due to the orbital mixing of p-states of the boron, the d-band centre of the palladium is shifted down, hence weakening its chemisorption.

In addition to being used for assessing the surface–adsorbate interaction, and strain-alloying effect, DFT has also been used to predict the propensity of light-element accommodation to be interstitial or substitutional, thereby allowing prediction of new chemical and catalytic properties. For example, the experimental report by Ma *et al.*[55] showed that doping boron into copper improves catalytic stability for the hydrogenation of dimethyl oxalate; however the experimental structure still remains uncharacterised. Mushrif *et al.* used DFT calculations to correlate the stable microstructure of Cu–B with catalytic performance.[56]

It was found by calculating the binding energy of boron at different sites on the Cu(111) surface that the most stable site is the octahedral site of the first subsurface layer (-486 kJ mol^{-1}). As previously indicated, the role of light elements such as boron or carbon in the palladium subsurface can significantly promote catalytic performance. DFT was also used by Illas *et al.* to investigate C incorporation in subsurface sites of Cu, Ag and Au by using a supercell slab model and a well-shaped nanoparticle model.[57] They reported that the most stable carbon site for the (111) surfaces of Cu and Ag is at the interstitial site, which is also true for their nanoparticle. In contrast, for the Au(111) slab surface, carbon is most stable chemisorbed on the surface, rather than integrated into the structure. For Au NPs however, carbon becomes more stable at the interstitial sites, which is partially due to the low coordination of the site in this morphology.

Catalytic applications

So far, we have demonstrated that incorporating light elements with metal NPs, either at interstitial or substitutional sites, may lead to structural distortion that modifies the surface structure and electronic properties of the host metal system, hence offering a way to tune the surface interactions between reactants and catalyst. In particular, interstitial doping may provide a new method for electronic modification of the metal surface. Herein, the recent studies of H-, Li-, B-, C-, and N-metal nanocatalysts will be summarised. As mentioned before, if the size of the dopant permits, it is energetically preferable for it to occupy interstitial sites rather than substitutional sites. However, examples of substitutional doping have been also reported for catalytic applications. We will highlight their unique catalytic properties accordingly.

Boron doping

It is well known that boron is an effective promotor for tuning the catalytic activity of a wide range of metal and non-metal systems.[58,59] In general, boron occupies the interstitial site of a host metal, but substitutional doping has also been reported in literature.[60] Pd–$^{\text{int}}$B is the most reported interstitial solid-solution system and has been used in electrochemistry and selective hydrogenation. Benefitting from the recent progress in synthesis strategies and characterisation, the Pd : B atomic ratio can be precisely controlled, approaching a boron mole fraction of 0.18.[61] In addition, Ni–$^{\text{int}}$B and Co–$^{\text{int}}$B systems are attracting attention as new catalysts for some important chemical conversions.

Methane dry reforming. Methane dry reforming is an important reaction which involves the conversion of methane into syn-gas (CO and H_2).[62] The conventional transition-metal-based catalysts are supported nickel or cobalt, but they suffer from rapid deactivation, for instance by coking in which carbon species accumulate and block the active sites. In DFT calculations reported by Saeys *et al.*,[63,64] boron atoms preferentially occupy the octahedral sites in the first subsurface layer of nickel, which weakens the binding strength of on-surface carbon and reduces the deposition of the resilient carbon species. Furthermore, occupancy of boron at subsurface sites was calculated to reduce the energy barrier of the methane activation from 91 to 64 kJ mol^{-1} through surface reorganisation caused by attractive boron–boron interactions.[65] The validity of the theoretical concept was subsequently confirmed by the experimental results, reported by Matralis *et al.*[66] Boron can also be incorporated into the subsurface layer of cobalt, as suggested by DFT calculations.[67] Recently, Takanabe *et al.* experimentally showed that the addition of boron to supported Co NPs by a wet chemical method can enhance CH_4 and CO_2 activation (Fig. 6a).[51] Their DFT simulations also indicated that boron atoms are preferentially located at the Co(100) facet of the NP, resulting in significant structural reorganisation (Fig. 6b). Boron atoms are also likely to incorporate into the topmost layer, but there they are more likely to be oxidised to form boron oxide species.

Formic acid decomposition. Formic acid is considered to be one of the most promising hydrogen storage chemicals to replace traditional pressurisation or cryogenic liquefaction technology. Pd metal is often suggested as the primary facile heterogeneous catalyst to accelerate the decomposition of

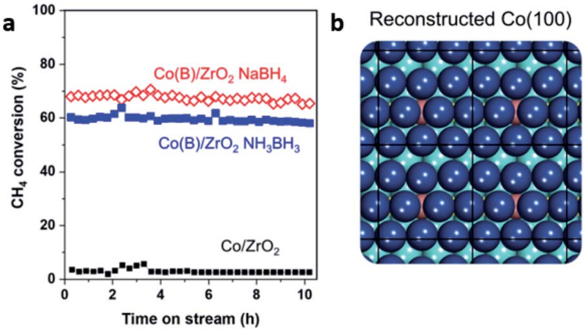

Fig. 6 (a) The reaction stream of methane conversion for Co/ZrO$_2$ and two Co–$^{\text{int}}$B/ZrO$_2$ catalysts prepared from NaBH$_4$ and NH$_3$BH$_3$. (b) Simulated surface reorganisation of Co (blue) induced by the presence of interstitial B (pink). This figure has been reproduced from ref. 51 with permission from Elsevier, copyright 2020.

formic acid, but it is limited by rapid catalytic deactivation induced by CO poisoning.[68] In 2014, Cai *et al.* reported that the use of Pd–^{int}B NPs obtained from a wet chemical reduction can boost the H_2 production from formic-acid/formate solutions at room temperature,[69] which opens a pathway for research on reversing the electro-hydrogenation process. The presence of boron can expand the Pd lattice, which strengthens the adsorption of formate ions and decreases the activation energy of the formic acid dehydration by changing the adsorption geometry for formic acid to an H-down orientation. Continuing from this work, Studt *et al.* used DFT calculations to investigate the effect of boron dopants on formic acid decomposition over a Pd catalyst. Boron was found to preferably occupy the octahedral sites of Pd(111), which formed the active site. The improved catalytic activity was attributed to the surface reorganisation that caused the destabilisation of CO* and COOH* on the metal surface, but strengthened the binding energies of oxygen-bound species (HCOOH* and OH*).[70]

Oxygen reduction reaction. The oxygen reduction reaction (ORR) is a very important reaction in hydrogen fuel cells.[71] Finding an alternative to Pt-based catalysts is highly essential because of their high cost. Pd catalysts alloyed with non-metallic elements, such as phosphorus,[50,72] can give superior catalytic activity to commercial Pt/C and Pd/C catalysts,[50,72] but the doped structure was amorphous, making characterisation and the correlation of structure to activity more difficult. In 2016, Sato *et al.* were the first to systematically test crystalline Pd–^{int}B NPs in the ORR. This catalyst was prepared by stepwise electroless deposition, instead of using traditional chemical wet synthesis strategies.[32] Successful catalyst preparation was verified by XRD and XPS (Fig. 7a and b).

Compared with commercial undoped Pd and Pt catalysts, crystalline Pd–^{int}B demonstrated 14-times and 35-times higher catalytic activity, respectively, as well as improved catalytic stability (Fig. 7c and d). The computational studies demonstrated that the presence of boron can lower the surface core level binding energy of Pd, indicating an increase in the density of states related to the Pd–O anti-bonding interaction with excess electrons from boron. The Pd–$O_{adsorbate}$ interaction is therefore weakened and hence the catalytic activity is boosted.

In the subsequent years, Cai *et al.*[73] and Wang *et al.*[74] reported that Pd–^{int}B catalysts can be prepared by different synthetic strategies which also exhibited high catalytic activity in the ORR. In the case of Wang *et al.* work, the concentration of boron can be controlled by adjusting the reaction temperature and precursor concentration (Fig. 7e). According to the DFT calculations reported by Wang *et al.*, they concluded that Pd–BO_2 assemblies and neighbouring palladium atoms are responsible for the superior catalytic activity; this effect is in addition to the effect of subsurface boron atoms. They also noted that other boron oxide species might exhibit good catalytic activity, even at low concentration (Fig. 7f).

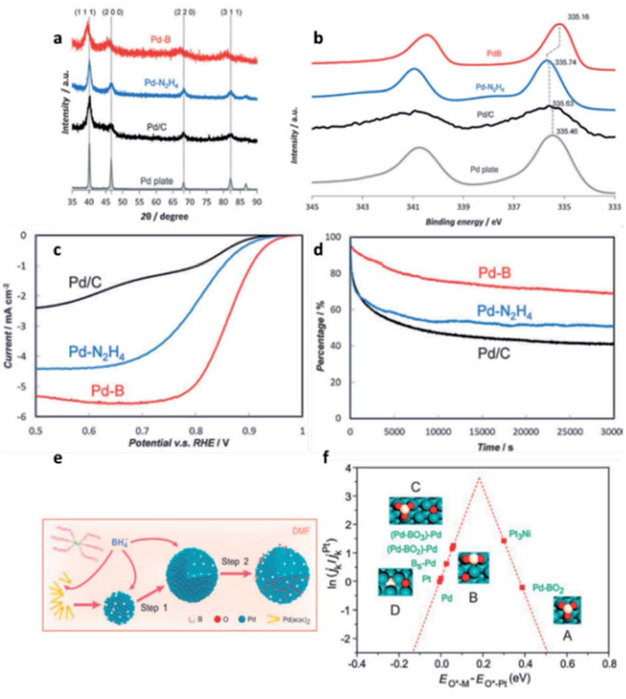

Fig. 7 (a) XRD, (b) XPS, (c) ORR polarisation curves, and (d) chronoamperometry responses (as percentage of initial current density) of Pd–^{int}B, Pd–N_2H_4, Pd/C and a Pd metal plate. This figure has been reproduced from ref. 32 with permission from Wiley-VCH, copyright 2016. (e) Illustration of the synthesis procedure for Pd–^{int}B/C. (f) ORR activity of different surface sites on the Pd–^{int}B surface, in comparison with platinum, with respect to the calculated O adsorption energies; This figure has been reproduced from ref. 74 with permission from American Chemical Society, copyright 2017.

Ethanol oxidation reaction. Direct ethanol fuel cells are one of the most promising future power sources owing to their advantages of facile storage, easy refuelling and the high power density of ethanol.[75] In comparison with Pt-based catalysts, Pd is a better choice for the ethanol oxidation reaction (EOR) in alkaline media. By incorporating light elements into Pd, the stability and activity can be significantly enhanced.[76] In 2019, Liu *et al.*[77] reported a novel synthetic method to obtain Pd–^{int}B mesoporous nanospheres (MNSs) in various particle size by a one-pot surfactant-templated aqueous colloidal synthesis. Dimethylamine borane and boric acid served as reducing agent and boron source, respectively, and dioctahecyldimethylammonium chloride (DODAC) was used as a surfactant template (Fig. 8a). Elemental mapping by EDX showed that the dispersion of boron is homogenous across the volume of the Pd MNSs (Fig. 8b). The presence of boron can enhance the electrocatalytic EOR performances in terms of mass and specific activities (Fig. 8c), in addition to the advantageous effect of the pore structure.

In 2020, the same group has continued to investigate the Pd–^{int}B binary system for EOR.[78] They suggested that the presence of boron can overcome charge-transfer resistances, and hence increase the rate of charge-transfer during the reaction. Furthermore, they attempted to rationalise the effect of boron on the Pd metal system in terms of electronic and bifunctional promotion (Fig. 8d). Incorporation of boron into metal lattices can not only modify the surface electronic properties of Pd by weakening the strength of adsorption of poisoning ethyoxy intermediates that are generated during the electrocatalytic

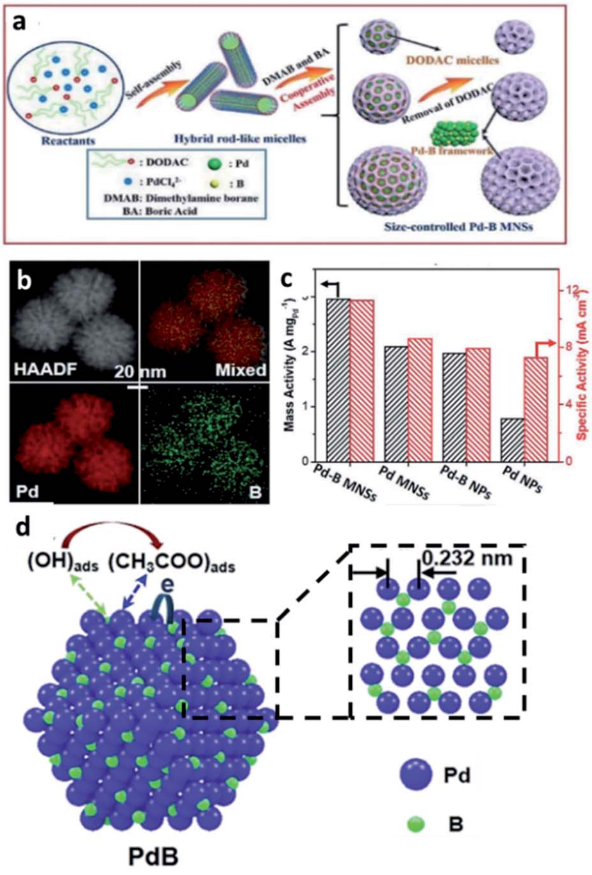

Fig. 8 (a) A scheme for the formation of Pd–^{int}B MNSs. (b) EDX elemental mapping; Pd (red), B (green). (c) Mass and specific activities of Pd–^{int}B MNSs, Pd MNSs, Pd–^{int}B NPs and commercial Pd NPs collected in 1.0 M KOH and 1.0 M ethanol. This figure has been reproduced from ref. 77 with permission from Royal Society of Chemistry, copyright 2019. (d) A illustration of electrocatalytic EOR on the surfaces of Pd–^{int}B. The inset shows the crystal structure of Pd–^{int}B: Pd (purple), B (green). This figure has been reproduced from ref. 78 with permission from American Chemical Society, copyright 2020.

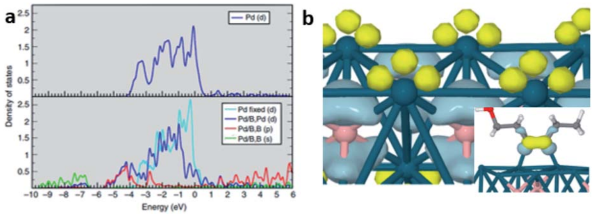

Fig. 9 DFT study of Pd–^{int}B system. (a) DOS of pure Pd (top) and Pd–^{int}B (bottom). (b) Electron-density difference isosurfaces show local electron-rich (light blue) and electron-poor regions (yellow) of Pd atoms (blue) with ^{int}B atoms (pink) due to states-mixing. Inset shows isolated HOMO/LUMO overlap of the adsorbate/surface interaction. This figure has been reproduced from ref. 37 with permission from Nature, copyright 2014.

EOR, but also facilitate the adsorption of OH–(B–OH$_{ads}$) which can accelerate the oxidation of the ethoxy intermediate and the associated diffusion away from the catalyst surface.

Selective hydrogenation of alkynes. Partial hydrogenation of alkynes to alkenes is an important reaction in the industrial field of organic synthesis,[79] since alkene-based compounds are the key feedstock for plastic production.[80] Unmodified Pd metal catalysts are unable to yield alkenes with high selectivity, owing to the presence of β-PdH$_x$ which can accelerate the conversion rate but causes over-hydrogenation.[81] The strategy of subsurface modification to tune selectivity can be dated back to 2008.[82] In 2014, our research group was first to modify the sublayer of Pd metals by incorporating B by using BH$_3$·THF in the partial hydrogenation of diphenylacetylene, phenylacetylene, and 3-hexyn-1-ol.[37] The selectivity to alkene products was much improved in comparison with the Lindlar catalyst, 5% PdPb/CaCO$_3$. As suggested by DFT calculations (Fig. 9a and b), the boron atoms occupied the thermodynamically-favourable octahedral sites. An effective overlap of d- and p-orbitals between boron interstitial atom and palladium resulted in reduced strength of adsorption for the alkene products, increasing the selectivity, in addition to blocking the formation of the unselective β-PdH$_x$ phase.

Nitrogen doping

Nitrogen is one of the most investigated elements for modifying nanomaterials.[83] The research of intermetallic nitride-based compounds has been summarised by Dongil[32] and Fan[84] *et al.* Unlike boron modifications, nitrogen requires the extreme conditions of high pressure to be alloyed with Pd metal.[85] In contrast, cobalt-based catalysts are often alloyed with nitrogen to enhance their catalytic activity. Monometallic cobalt NPs exhibit one of two possible phases, namely HCP and FCC, which are dependent on their size and the temperature employed in the preparation.[86] The cobalt HCP–FCC phase transition occurs at around 700 K.[87] Cobalt NPs with FCC phase are most commonly reported, which can be mainly attributed to the particle size effect. As illustrated by the work of Shimada *et al.*,[88] particles with FCC structure are energetically more stable below 20 nm.[89] Treatment with ammonia gas or other N-containing sources can incorporate nitrogen at the octahedral sites of cobalt, which can allow the formation of Co$_4$N; though to a lesser degree, nitrogen can also reside at the tetrahedral sites, leading to the formation of Co$_{5.47}$N and CoN. The type of interstitial hole that nitrogen occupies is governed by the synthetic method.

CO$_2$ hydrogenation. Hydrogenation of CO$_2$ to hydrocarbons is a useful chemical process for forming useful fuel products while removing a highly harmful greenhouse gas from the atmosphere. Effective non-noble-metal-based catalysts are in strong demand. Zeng *et al.* reported that the catalytic activity of Co nanosheets in CO$_2$ hydrogenation can be increased by 64-times by conversion to Co$_4$N by nitrogen incorporation (evaluated at 150 °C under 32 bar of H$_2$) (Fig. 10a).[90] The formation of Co$_4$N was verified by EDX mapping, XRD and XPS (Fig. 10b–d). The mechanistic studies demonstrated that Co$_4$N can transform into Co$_4$NH$_x$ by H adsorption on N atoms under H$_2$ pressure. The amido-hydrogen in Co$_4$NH$_x$ interacts with CO$_2$, leading to the formation of HCOO* intermediates. Further, the adsorbed

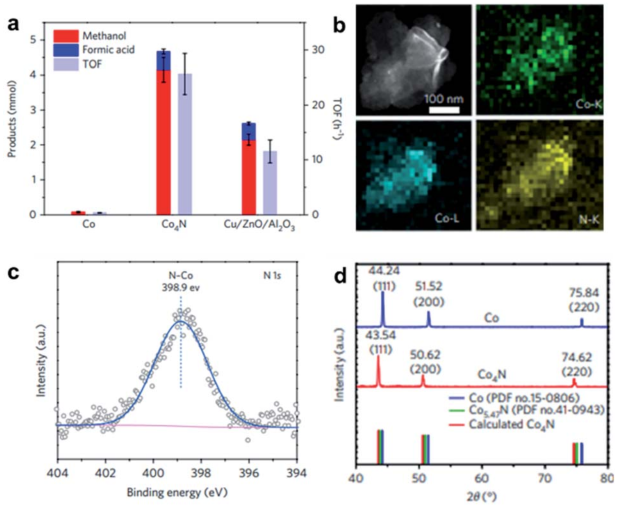

Fig. 10 (a) Product selectivity and TOF of Co nanosheets, Co_4N nanosheets and $Cu/ZnO/Al_2O_3$ in CO_2 hydrogenation under 32 bar of 1 : 3 CO_2/H_2 at 150 °C for 3 hours. (b) EDX elemental mapping of the Co K-, Co L- and N K-edges of Co_4N nanosheets. (c) N 1s XPS spectrum for Co_4N sheets. (d) XRD patterns of Co and Co_4N sheets. This figure has been reproduced from ref. 90 with permission from Nature, copyright 2017.

H_2O* was found to activate the amido-hydrogen atoms through the hydrogen bonding interaction, which promotes the hydrogenation process.

Methanation of carbon oxides. The methanation of carbon oxides (CO and CO_2) is an important chemical process for producing synthetic natural gas, for which Zhang *et al.* reported Co_4N to be a highly active and stable catalyst in comparison to pristine cobalt metal.[91] This catalyst showed high activity towards methane formation and achieved outstanding product selectivity (>98%) at 200–300 °C. Additionally, the catalyst was highly tolerant to sintering and carbon deposition shown by post-mortem catalyst characterisation (XRD, TEM and TGA analysis).

Oxygen reduction reaction. Interesting reports can be found on the application of the ORR using Co–^{int}N systems. Xia *et al.* reported that CoN/C NPs can be prepared by refluxing Co/C in a solution of *o*-xylene, followed by thermal annealing under ammonia. The modified Co catalyst exhibited higher ORR activity and stability in an alkaline environment compared with commercial Pt/C, exhibiting an onset potential of 0.85 V *vs.* RHE.[92] Nøskov and Siahrostami *et al.* investigated the effect of the structure of CoN on catalytic activity by conducting DFT calculations on the rock salt and zinc blende structures.[93] The authors suggested that the presence of a cobalt oxide layer on CoN could lower the over-potential significantly. In particular, the (111) facet of CoN with a layer of CoO was considered to be the most active surface for the ORR. Additionally, Zhang *et al.* reported that CoN decorated on nitrogen-doped graphene exhibited exemplary stability and methanol tolerance under acidic conditions.[94]

In the same year, Wang *et al.* evaluated $Co_{5.47}N$ supported on porous nitrogen-doped carbon for the application of ORR. This system can exhibit an acceptable catalytic activity, with an onset potential of −42 mV *vs.* SCE.[96] Huang *et al.* later reported that conducting a single-step preparation increased the activity of the catalyst.[97] Sun *et al.*[98] and Wu *et al.*[99] synthesised $Co_{5.47}N$ in complex architectures by adding a third component. They concluded that the interaction between N and Co can enhance the catalytic activity. Additionally, Hou *et al.* reported that FeN (zinc blende structure) catalysts can be bound onto nitrogen-doped graphene through π–π stacking and oxygen-containing functional groups. Interaction between the support and the Fe–^{int}N catalyst can result in a synergistic effect which enhances the catalytic activity and stability.[100]

Oxygen evolution reaction. The oxygen evolution reaction (OER) is one of the essential processes for hydrogen production in water splitting and rechargeable metal–air batteries.[101,102] In 2016, Fan *et al.* demonstrated a time-efficient (3 minute) N_2 radio-frequency plasma treatment to obtain CoN nanowire, in which N occupies the interstitial sites.[95] The formation and morphology of CoN nanowire was verified by XRD, XPS and TEM (Fig. 11). In comparison with other catalysts, CoN-based nanomaterials exhibit superior activity in OER, as shown by a lower overpotential at 10 mA cm^{-2}, a smaller Tafel slope, and better stability in an alkaline solution. Subsequently, Yang *et al.* have reported that ultrafine CoN nanoparticles (5 nm) decorated on carbon nanotubes exhibited a similar activity to the work by Fan *et al.*[103]

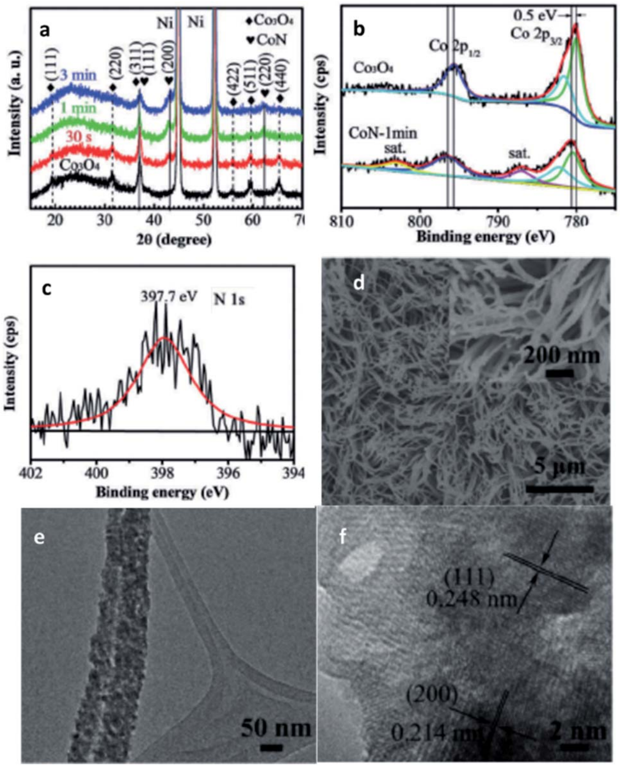

Fig. 11 Characterisation of CoN. (a) XRD of Co_3O_4 and CoN. XPS spectra: (b) Co 2p of Co_3O_4 and CoN-1 min, (c) N 1s of CoN. (d) SEM, (e) TEM, (f) HR-TEM micrograph of CoN. This figure has been reproduced from ref. 95 with permission from Wiley-VCH, copyright 2016.

Carbon doping

In the field of ferrous metallurgy, carbon is an essential element that can be alloyed into octahedral holes in the Fe bcc lattice, making the steel harder and stronger.[29] In contrast, carbonaceous species are often considered poisonous in catalytic applications due to active site blocking. However, recent investigations have demonstrated that carbon can also play a promoting role in catalysis, namely when it resides in the subsurface of the metal catalyst. The subsurface modification of Pd by carbon (the maximum molar fraction is up to 0.13)[81] has been the subject of intense research within the field, and will be summarised in the section below. Recent works also report that this strategy has been applied to other mono-[40] and bimetallic[104] systems.

Selective hydrogenation of alkyne. As discussed in the previous chapter, Pd NPs have been interstitially doped with carbon for the selective hydrogenation of alkynes.[82] Teschner *et al.*[105] showed by XAS that the presence of carbon inhibits the formation of the unselective β-hydride phase; this is analogous to the behaviour of Pd–^{int}B, discussed above.[37] Inspired by Schlogl's work,[82] our research group reported a green synthetic preparation of Pd–^{int}C for partial hydrogenation of 3-hexyn-1-ol and 4-octyne to their respective alkene products at ultra-high selectivity.

In comparison with the Lindlar type catalyst, the subsurface modified Pd–^{int}C NPs can suppress undesirable isomerisation and over-hydrogenation, which is attributed to the effects from the hybridisation of the Pd d-orbital with the C sp-orbital.[30]

In 2019, Jin *et al.* reported the successful preparation of a Pd–^{int}C nanocrystal based on our synthesis strategy and widened the application to other substrates.[106] This strategy has also been applied to other transition-metal catalysts, such as Au. Recently, Wan *et al.* have reported that carbon can be interstitially doped into Au for selective hydrogenation of alkyne-based substrates.[40] Though the XRD did not reveal any lattice variation, they speculated that the location of carbon is at the interstitial sites, as reflected by the XPS and XANES (Fig. 12a and b). The TOF value of the Au–^{int}C NPs was found to be higher than undoped Au/TiO$_2$ with a similar particle size (Fig. 12c). A linear relationship between the activation energy and entropy of activation was observed (Fig. 12d). Their DFT calculations indicated that the activation barrier of hydrogen dissociation can be reduced to 0.59 eV on Au–^{int}C(111), and showed that doping affects the adsorption modes of 3-nitrosytrene (Fig. 12e and f).

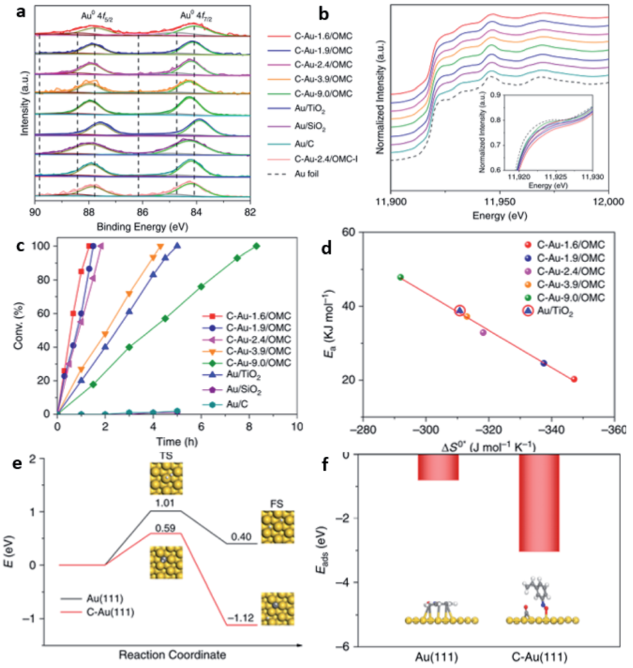

Fig. 12 (a) Au 4f XPS and (b) Au L$_3$-edge XANES spectra for various Au–^{int}C NPs decorated on ordered mesoporous carbon. (c) The conversion of 3-nitrostyrene over different ctatalysts. (d) The resulting correlation between the activation energy (E_a) and entropy of activation ($\Delta S^{\circ *}$). (e) DFT calculations of energy profiles for the dissociation of H$_2$ on pristine Au(111) and Au–^{int}C(111), and (f) corresponding absorption modes. This figure has been reproduced from ref. 40 with permission from Nature, copyright 2020.

Hydrogen doping

Historically, the study of metal hydrides has focussed on their application in hydrogen storage. However, recently hydrogen has also been found to be a promising element to incorporate into metal systems to tune their catalytic activity. Recently, palladium hydride (Pd–^{int}H), an interstitial metal hydride,[107] has increasingly received attention for a wide range of catalytic applications. There are two well-known structures of Pd–^{int}H: the α-phase that has a composition of approximately PdH$_{0<x\leq 0.03}$ and exhibits a slightly higher lattice parameter than pure palladium (3.889 Å), and the β-phase that has a composition of approximately PdH$_{x\geq 0.58}$, whose formation is observed by a sudden increase in lattice parameter to 4.018 Å.[108] Sometimes, α-PdH$_x$ and β-PdH$_x$ phases can coexist in the region of the phase diagram(0.03 ≤ x ≤ 0.58).[109,110] The distribution between the octahedral and tetrahedral sites has been shown to be dependent on the depth from the surface, and hence highly dependent on particle size and shape.[48] Elsewhere it has been found by NPD that the occupancy of tetrahedral sites in both the α- and β-phases increases when the host Pd framework is alloyed with other metals.[111] Recent work on the utilisation of Pd/C in the electro-hydrogenation of dinitrogen demonstrated that the *in situ* formation of Pd–^{int}H can catalyse the hydrogenation.[112] Herein, other recent catalytic applications are detailed.

Methanol oxidation reaction. In 2015, Huang *et al.* reported that thermodynamically stable and catalytically active β-PdH$_{0.43}$ NPs can be prepared by a one-step synthesis.[113] They initially prepared Pd NPs with various shapes (nano-polycrystals, nano-tetrahedra and nano-cubes) based on a reported method,[114] and then converted them to β-PdH$_{0.43}$ (Fig. 13a–f). The nano-polycrystals and nano-tetrahedra supported on carbon both with and without hydride were tested in the electrocatalytic methanol oxidation reaction (MOR) in an alkaline medium. The hydride-compound exhibited higher activity than the pristine Pd catalyst (1.228 mA cm^{-2} *vs.* 0.886 mA cm^{-2}), which can be

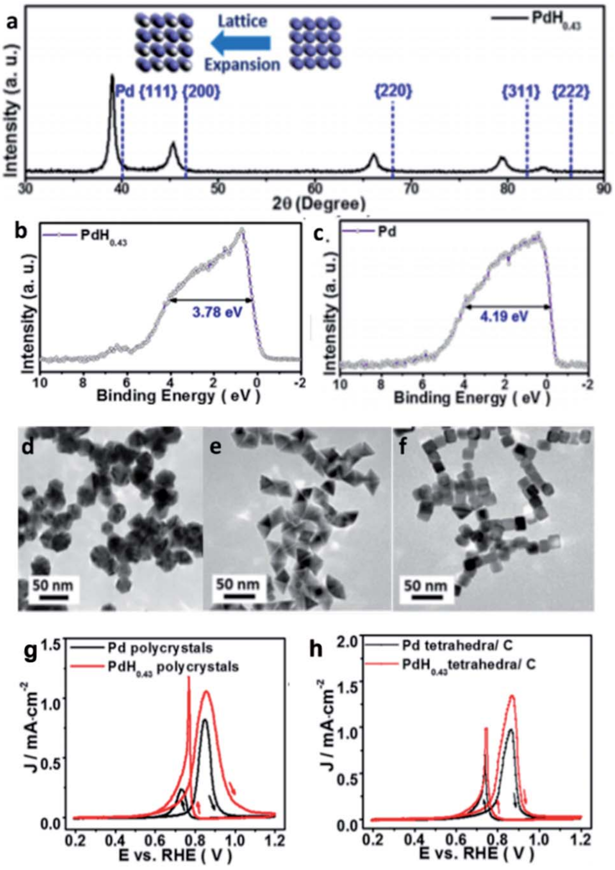

Fig. 13 (a) XRD of $PdH_{0.43}$. Valence band structure of (b) $PdH_{0.43}$ and (c) Pd. (d–f) TEM micrographs of $PdH_{0.43}$ nano-polycrystals, nano-tetrahedra and nanotubes. Cyclic voltammetry of Pd and $PdH_{0.43}$ (g) polycrystals and (h) tetrahedra in N_2 saturated, 0.1 M KOH with 0.1 M methanol, scan rate of 10 mV s^{-1}. This figure has been reproduced from ref. 113 with permission from American Chemical Society, copyright 2015.

attributed to the weaker CO binding on $PdH_{0.43}$ (Fig. 13g and h). In 2019, Choi *et al.* prepared (100)-faceted β-$PdH_{0.4}$ cubes and (111)-faceted β-$PdH_{0.4}$ octahedra to investigate the correlation between the catalytic performance and shape/facet/composition. Again, the presence of hydrogen at interstitial sites can increase the catalytic activity and stability, which is the consequence of shifting the d-band centre down from the Fermi level with respect to the unmodified Pd system. Furthermore, the β-$PdH_{0.4}$ cubes showed the highest MOR activity among the catalysts.[115] In 2020, Li *et al.* employed machine learning of stochastic surface walking to find the Pd–^{int}H surface that yielded the lowest energy pathway.[116] They found that at high hydrogen pressure the well-defined phases Pd_2H and Pd_4H_3 appeared. They suggested that α-phase $PdH_{0.03}$ is simply pure Pd with a surface covering of hydride, and that the β-phase $PdH_{0.03}$ is a mixture of Pd_2H and Pd_4H_3. The surface that yields the highest selectivity was predicted to be Pd(111) and the poorest to be Pd_4H_3(100), which was supported by their experimental results, in which selectivity was increased by increasing particle size to diminish the Pd_4H_3(100). It was also suggested that bimetallic alloys of palladium, such as PdAg, have increased selectivity due to the inhibition of the Pd_4H_3 phase.

Formic acid oxidation. In 2016, Xie *et al.* reported that Pd–^{int}H can be prepared by treating commercial Pd/C with *n*-butylamine at relatively mild temperatures. The catalyst was stable and exhibited a low over-potential for formic acid electro-oxidation, with an oxidation peak potential of 0.04 V *vs.* SCE, superior to that of commercial Pd black.[117] Subsequently, Choi *et al.* showed that $PdH_{0.4}$ nanomaterials with various morphologies also achieved good catalytic performance in formic acid oxidation.[115]

Nitrogen reduction reaction. In 2020, Chen *et al.*[118] reported that nanoporous $PdH_{0.43}$ can be used in the nitrogen reduction reaction (NRR). It was synthesised by chemical dealloying of the bimetallic alloy $Al_{80}Pd_{20}$, followed by *in situ* H_2 injection, and verified by XRD and XPS. Before conducting the catalytic testing, the chronoamperometry tests of the catalyst was studied at various potentials (Fig. 14a), demonstrating good stability of the catalyst. The catalyst exhibited a TOF value of 91.5 h^{-1} mg^{-1} with a faradic efficiency of 43.6% at −0.15 V, which is approximately three-times higher than that of nanoporous Pd (Fig. 14b and c). Additionally, an experiment involving isotopically-labelled dinitrogen suggested that hydrogen from the $PdH_{0.43}$ surface initiates the activation process (Fig. 14d and e). With the aid of DFT calculations (Fig. 14f), they suggested that $*N_2H$ formation is the rate-limiting step, and that the energy barrier of $*N_2H$ formation is lower in the presence of nanoporous Pd–^{int}H (0.65 eV) in comparison to pure nanoporous Pd (0.91 eV).

Oxygen reduction reaction. Similar to the Co–^{int}N system, Pd–^{int}H was found to be an effective catalytic system in the ORR. Wang *et al.* prepared Pd–^{int}H nanocubes encapsulated within

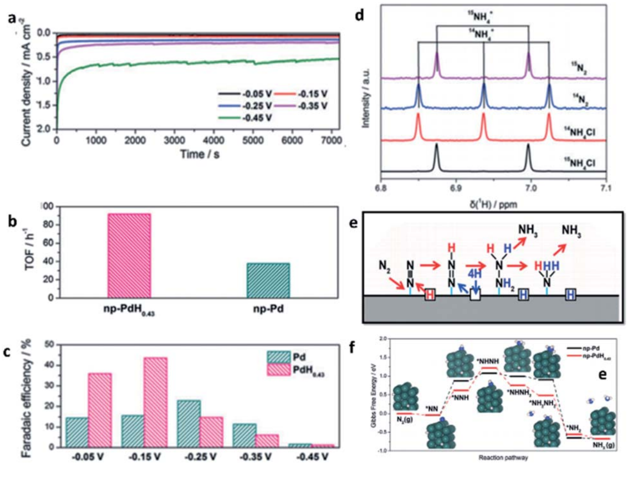

Fig. 14 (a) Potentiostatic curves of np-$PdH_{0.43}$ during NRR. (b) TOF of np-Pd and np-$PdH_{0.43}$ at −0.15 V. (c) Faradaic efficiencies at selected potentials. (d) Baseline-subtracted ^{1}H-NMR spectra of the post-mortem electrolyte with $^{15}N_2$ and $^{14}N_2$ and the reference $^{14}NH_4Cl$ and $^{15}NH_4Cl$. (e) Proposed reaction pathway for nitrogen reduction. (f) Gibbs free-energy profiles of the NRR on np-Pd and np-$PdH_{0.43}$. This figure has been reproduced from ref. 118 with permission from Wiley-VCH, copyright 2020.

2D amorphous Ni–B nanosheets. It was found that the stability and catalytic activity can be tuned by the H occupancy of the interstitial site of Pd.[119] The ORR activity of $PdH_{0.706}$@Ni–B at 0.90 V *vs.* RHE yielded a current density of 1.05 A mg^{-1}, which was approximately 5-times higher than Pt/C (0.21 A mg^{-1}). Based on Wang's result, Song *et al.*[120] synthesised Pd–^{int}H nanodendrites, which showed good stability and high catalytic activity as well.

***N*-Alkylation.** Fu *et al.* reported that Pd–^{int}H supported on Al_2O_3 can be used for *N*-alkylation of amines with phenols, which progresses by tandem hydrogenation and amination reaction, resulting in high yields with good stereoselectivity under mild conditions.[121]

Lithium doping

Lithium doping is well-known to significantly modify the catalytic properties of metal oxide systems. A typical example, is the use of Li–MgO in oxidative methane coupling (OMC), in which C_2 products are produced at high yields by the coupling of methyl radicals under high temperatures (943–1223 K);[122] without Li no such catalysis is seen. However, there have been very limited works shown from recent open literature on using lithium doping in transition metal systems catalysis under reducing environments. Though the recent review on the catalytic reactions of light-element doped palladium by Rioux *et al.*[123] was largely comprehensive, they did not include any mention of lithium-doped Pd. Despite limited examples, highlight of these reports are presented below.

Selective hydrogenation of alkyne. As stated cationic Li is small enough to be placed in the interstitial hole, but neutral Li is too large for interstitial accommodation, hence favouring substitutional modification on the crystal surface. For instance, our research group reported that Pd–^{int}Li NPs can be prepared by the thermal decomposition of $Li(OAc)\cdot 2H_2O$ in the presence of Pd/C. The presence of cationic Li at the interstitial site, caused by the large difference in electronegativity between Li and Pd, can almost totally inhibit the formation of the unselective β-hydride phase, which would facilitate over-hydrogenation beyond the more valuable alkene products.[124]

Ammonia synthesis from N_2/H_2. Ruthenium is an effective catalyst for Haber–Bosch thermal ammonia synthesis from N_2/H_2.[125] Doping Ru with Li species has recently been shown by our research group[126] to confer the strongest promotion effect in comparison to other alkali and alkaline earth metal dopants (Fig. 15a). Li has no significant p- or d-orbital character, but can reduce the metal framework *via* mixing of p- or d-orbitals, causing a downshift of the Ru d-band; this is analogous to the behavior of $[Ca_{24}Al_{28}O_{64}]^{4-}(e^-)_4$ electride.[127] In addition to electronic promotion of the ruthenium metal, Li can also act as a structural promoter. Exposed substitutionally doped Li on the surface can selectively block the N_2 dissociation step-site as well as stabilising the partially negatively charged dinitrogen-containing intermediates and associated transition states on the terrace sites (Fig. 15b). Thus, the remarkable low-pressure ammonia synthesis rate is attributed to the electronic promotion and surface stabilisation by Ru–^{sub}Li.

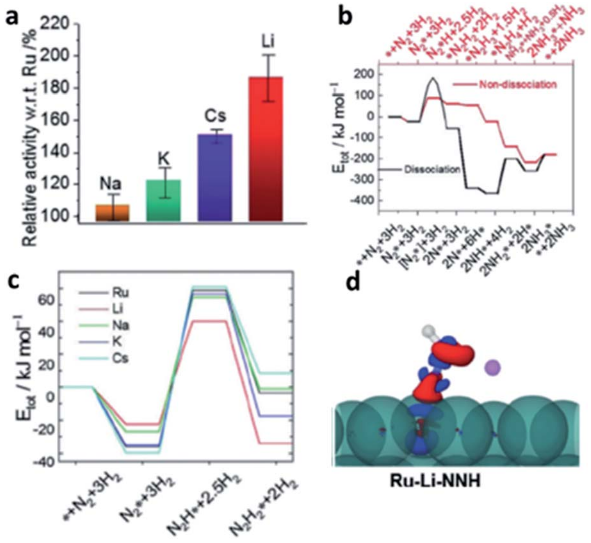

Fig. 15 (a) Ammonia synthesis activity of various alkali-metal ion promoted Ba–Ru/AC with respect to total Ru content. (b) Calculated energy diagrams for ammonia synthesis *via* dissociative and associative pathways on Ru{0001} surface; the binding energy, E_{tot}, is defined relative to the energies for the free Ru{0001} surface (*). Structures of the most stable intermediates are shown above and below the energy diagram for dissociative pathway and associative pathway. (c) Calculations for the most energetic step of adsorbed N_2* to N_2H* on Ru {0001} terrace with various dopants. (d) Electron-density difference plot ($\rho_{total} - \rho_{Ru} - \rho_{NNH}$, where ρ is the electron density of the subscript component); negative (blue), positive (red), which shows the asymmetrical surface polarisation and stabilisation of NNH species by Li^+ (purple) to induce electron back donation to π* region from Ru. This figure has been reproduced from ref. 126 with permission from Wiley-VCH, copyright 2020.

DFT modelling was also used to further investigate the stabilisation of adsorbed N_2 and hydrogenated species by surface alkali atoms by the associative pathway on terrace Ru sites. There is a particularly strong structural stabilisation for Li to stay closer to δ-N_2*H than for any other alkali dopant (Fig. 15c). It is interesting to note from the calculated electron-density difference plots in Fig. 15d that the polarisation of the surface by Li can clearly break the symmetry of N_2H* and greatly promote the back donation of Ru to N_2H* (to give δ^- charge) compared to the unpromoted Ru. This step facilities the associative mechanism for ammonia synthesis.

Dehydrogenation reaction. Ag can be substituted by Li due to the smaller difference in their electronegativity and atomic radii; this is observed by a contraction of the Ag lattice.[128] Additionally, below the equimolar AgLi composition, alloy structures of approximate composition Ag_5Li have been used in catalysis applications,[129,130] but structurally seem to be largely uninterrogated. It is these types of non-stoichiometric doped structures that are often active as discussed extensively above.

Conclusions

Overall, we have summarised the recent contributions to several light-element-modified transition-metal systems, discussing their synthesis, characterisation and the relationship between structure and catalytic applications and performance. In contrast to substitutional systems, interstitial light-element modified systems have wide-reaching application across catalysis and hold tremendous appeal across the community.

There is no doubt that the chemistry of light-element-modified transition-metal systems will continue to flourish and pave an avenue to replace precious, expensive, and often more toxic transition-metal based catalysts. However, the research about the construction of such nanomaterials is still limited. For instance, the syntheses of nanoscale materials are challenging by conventional strategies. Incorporation of light-elements using recent synthetic methodologies such as forming multi-component alloy nanoparticles by fast non-equilibrium heating of their aerosols could be an exciting direction.[128] On the other hand, some advanced structural characterisation techniques are still in the early stages of development and are difficult to access. These issues are being addressed in the continued development of advanced techniques and more facile synthesis procedures, which opens the way for light-element-modified transition-metal systems to play an increasingly important role in heterogeneous catalysis.

Conflicts of interest

There are no conflicts to declare.

Acknowledgements

The first and second author thank for the care from their families and friends during the pandemic period of COVID-19.

Notes and references

1 G. Bond, *Heterogeneous catalysis: principles and applications*, Oxford: Clarendon Press, Oxford, 1982, vol. 27.
2 B. Huang, H. Kobayashi, T. Yamamoto, T. Toriyama, S. Matsumura, Y. Nishida, K. Sato, K. Nagaoka, M. Haneda, W. Xie, Y. Nanba, M. Koyama, F. Wang, S. Kawaguchi, Y. Kubota and H. Kitagawa, *Angew. Chem., Int. Ed.*, 2019, **58**, 2230–2235.
3 A. M. Alexander and J. S. J. Hargreaves, *Chem. Soc. Rev.*, 2010, **39**, 4388–4401.
4 R. B. Levy and M. Boudart, *Science*, 1973, **181**, 547–549.
5 E. W. McFarland and H. Metiu, *Chem. Rev.*, 2013, **113**, 4391–4427.
6 T. Chen, I. Ellis, T. J. N. Hooper, E. Liberti, L. Ye, B. T. W. Lo, C. O'Leary, A. A. Sheader, G. T. Martinez, L. Jones, P.-L. Ho, P. Zhao, J. Cookson, P. T. Bishop, P. Chater, J. V. Hanna, P. Nellist and S. C. E. Tsang, *J. Am. Chem. Soc.*, 2019, **141**, 19616–19624.
7 K. D. Gilroy, A. Ruditskiy, H.-C. Peng, D. Qin and Y. Xia, *Chem. Rev.*, 2016, **116**, 10414–10472.
8 M. Beck, M. Ellner and E. J. Mittemeijer, *Mater. Sci. Forum*, 2000, **321–324**, 604–609.
9 P. K. Liao, K. E. Spear and M. E. Schlesinger, *J. Phase Equilib.*, 1996, **17**, 340–345.
10 Z. Peng and H. Yang, *Nano Today*, 2009, **4**, 143–164.
11 S. Furukawa and T. Komatsu, *ACS Catal.*, 2017, **7**, 735–765.
12 R. Ferrando, J. Jellinek and R. L. Johnston, *Chem. Rev.*, 2008, **108**, 845–910.
13 J. Maier, *J. Inorg. Gen. Chem.*, 2017, **643**, 2083–2087.
14 Y. M. Zhang, J. R. G. Evans and S. Yang, *J. Cryst. Phys. Chem.*, 2013, **44**, 81–97.
15 M. Armbrüster, *Encyclopedia of Catalysis*, John Wiley & Sons, Inc., Hoboken, NJ, USA, 2011.
16 Y. An, H. Ijaz, M. Huang, J. Qu and S. Hu, *Dalton Trans.*, 2020, **49**, 1646–1651.
17 E. W. McFarland and H. Metiu, *Chem. Rev.*, 2013, **113**, 4391–4427.
18 A. Machocki and R. Jezior, *Chem. Eng. J.*, 2008, **137**, 643–652.
19 M. Armbrüster, R. Schlögl and Y. Grin, *Sci. Technol. Adv. Mater.*, 2014, **15**, 034803.
20 P. Chen, E. Akiba, S. Orimo, A. Zuettel and L. Schlapbach, *Hydrogen Science and Engineering: Materials, Processes, Systems and Technology*, Wiley-VCH Verlag GmbH & Co. KGaA, Weinheim, Germany, 2016, pp. 763–790.
21 Y. Xiao, J.-Y. Hwang and Y.-K. Sun, *J. Mater. Chem. A*, 2016, **4**, 10379–10393.
22 S. Carenco, D. Portehault, C. Boissière, N. Mézailles and C. Sanchez, *Chem. Rev.*, 2013, **113**, 7981–8065.
23 A. B. Dongil, *Nanomaterials*, 2019, **9**, 1111.
24 G. Hägg, *Phys. Chem. B*, 1931, **12**, 33.
25 L. H. Bennett, A. J. McAlister and R. E. Watson, *Phys. Today*, 1977, **30**, 34–41.
26 L. Brewer, *Science*, 1968, **161**, 115–122.
27 S. T. Oyama, *Catal. Today*, 1992, **15**, 179–200.
28 J. S. Galsin, in *Impurity Scattering in Metallic Alloys*, Springer US, Boston, MA, 2002, pp. 93–123.
29 P. Atkins, F. Armstrong, T. Overton, J. Rourke and M. Weller, *Inorganic Chemistry*, OUP, Oxford, 5th edn, 2009.
30 C. W. A. Chan, K. Y. Tam, J. Cookson, P. Bishop and S. C. Tsang, *Catal. Sci. Technol.*, 2011, **1**, 1584.
31 A. L. Bugaev, A. A. Guda, I. A. Pankin, E. Groppo, R. Pellegrini, A. Longo, A. V. Soldatov and C. Lamberti, *Catal. Today*, 2019, **336**, 40–44.
32 T. T. Vo Doan, J. Wang, K. C. Poon, D. C. L. Tan, B. Khezri, R. D. Webster, H. Su and H. Sato, *Angew. Chem., Int. Ed.*, 2016, **55**, 6842–6847.
33 M. Nesselberger and M. Arenz, *ChemCatChem*, 2016, **8**, 1125–1131.
34 F. M. Ross, *Science of Microscopy*, Springer, New York, NY, 2007, pp. 445–534.
35 Z. Wang, D. Santhanagopalan, W. Zhang, F. Wang, H. L. Xin, K. He, J. Li, N. Dudney and Y. S. Meng, *Nano Lett.*, 2016, **16**, 3760–3767.
36 K. Kobayashi, H. Kobayashi, M. Maesato, M. Hayashi, T. Yamamoto, S. Yoshioka, S. Matsumura, T. Sugiyama, S. Kawaguchi, Y. Kubota, H. Nakanishi and H. Kitagawa, *Angew. Chem., Int. Ed.*, 2017, **56**, 6578–6582.
37 C. W. A. Chan, A. H. Mahadi, M. M.-J. Li, E. C. Corbos, C. Tang, G. Jones, W. C. H. Kuo, J. Cookson, C. M. Brown,

P. T. Bishop and S. C. E. Tsang, *Nat. Commun.*, 2014, **5**, 5787.

38 H. Yang, R. N. Rutte, L. Jones, M. Simson, R. Sagawa, H. Ryll, M. Huth, T. J. Pennycook, M. L. H. Green, H. Soltau, Y. Kondo, B. G. Davis and P. D. Nellist, *Nat. Commun.*, 2016, **7**, 12532.

39 K. Okitsu, Y. Mizukoshi, H. Bandow, T. A. Yamamoto, Y. Nagata and Y. Maeda, *J. Phys. Chem. B*, 1997, **101**, 5470–5472.

40 Y. Sun, Y. Cao, L. Wang, X. Mu, Q. Zhao, R. Si, X. Zhu, S. Chen, B. Zhang, D. Chen and Y. Wan, *Nat. Commun.*, 2020, **11**, 4600.

41 T. Fujii, *Am. Mineral.*, 1960, **45**, 370–382.

42 A. L. Bugaev, O. A. Usoltsev, A. Lazzarini, K. A. Lomachenko, A. A. Guda, R. Pellegrini, M. Carosso, J. G. Vitillo, E. Groppo, J. A. van Bokhoven, A. V. Soldatov and C. Lamberti, *Faraday Discuss.*, 2018, **208**, 187–205.

43 W. Jones, P. P. Wells, E. K. Gibson, A. Chutia, I. P. Silverwood, C. R. A. Catlow and M. Bowker, *ChemCatChem*, 2019, **11**, 4334–4339.

44 K. Jiang, J. Chang, H. Wang, S. Brimaud, W. Xing, R. J. Behm and W.-B. Cai, *ACS Appl. Mater. Interfaces*, 2016, **8**, 7133–7138.

45 D. S. Su, B. Zhang and R. Schlögl, *Chem. Rev.*, 2015, **115**, 2818–2882.

46 S. Yamashita, J. Kikkawa, K. Yanagisawa, T. Nagai, K. Ishizuka and K. Kimoto, *Sci. Rep.*, 2018, **8**, 12325.

47 B. Lin, X. Wu, L. Xie, Y. Kang, H. Du, F. Kang, J. Li and L. Gan, *Angew. Chem., Int. Ed.*, 2020, **59**, 20348–20352.

48 H. Akiba, M. Kofu, H. Kobayashi, H. Kitagawa, K. Ikeda, T. Otomo and O. Yamamuro, *J. Am. Chem. Soc.*, 2016, **138**, 10238–10243.

49 T. Ishimoto and M. Koyama, *J. Chem. Phys.*, 2018, **148**, 034705.

50 K. C. Poon, D. C. L. Tan, T. D. T. Vo, B. Khezri, H. Su, R. D. Webster and H. Sato, *J. Am. Chem. Soc.*, 2014, **136**, 5217–5220.

51 A. J. Al Abdulghani, J. Park, S. M. Kozlov, D.-C. Kang, B. AlSabban, S. Pedireddy, A. Aguilar-Tapia, S. Ould-Chikh, J.-L. Hazemann, J.-M. Basset, L. Cavallo and K. Takanabe, *J. Catal.*, 2020, **392**, 126–134.

52 F. Studt, F. Abild-Pedersen, T. Bligaard, R. Z. Sørensen, C. H. Christensen and J. K. Nørskov, *Angew. Chem., Int. Ed.*, 2008, **47**, 9299–9302.

53 P. Wu and B. Yang, *Phys. Chem. Chem. Phys.*, 2016, **18**, 21720–21729.

54 M. Mavrikakis, B. Hammer and J. K. Nørskov, *Phys. Rev. Lett.*, 1998, **81**, 2819–2822.

55 S. Zhao, H. Yue, Y. Zhao, B. Wang, Y. Geng, J. Lv, S. Wang, J. Gong and X. Ma, *J. Catal.*, 2013, **297**, 142–150.

56 Q. T. Trinh, A. Banerjee, Y. Yang and S. H. Mushrif, *J. Phys. Chem. C*, 2017, **121**, 1099–1112.

57 O. Piqué, I. Z. Koleva, F. Viñes, H. A. Aleksandrov, G. N. Vayssilov and F. Illas, *Angew. Chem., Int. Ed.*, 2019, **58**, 1744–1748.

58 T. Koretsune and S. Saito, *Phys. Rev. B*, 2008, **77**, 165417.

59 S. Agnoli and M. Favaro, *J. Mater. Chem. A*, 2016, **4**, 5002–5025.

60 H. Brodowsky and H. Sagunski, *Berichte der Bunsengesellschaft für physikalische Chemie*, 1983, **87**, 803–805.

61 M. Beck, M. Ellner and E. J. Mittemeijer, *Mater. Sci. Forum*, 2000, **321–324**, 604–609.

62 M. Akri, S. Zhao, X. Li, K. Zang, A. F. Lee, M. A. Isaacs, W. Xi, Y. Gangarajula, J. Luo, Y. Ren, Y.-T. Cui, L. Li, Y. Su, X. Pan, W. Wen, Y. Pan, K. Wilson, L. Li, B. Qiao, H. Ishii, Y.-F. Liao, A. Wang, X. Wang and T. Zhang, *Nat. Commun.*, 2019, **10**, 5181.

63 J. Xu and M. Saeys, *J. Catal.*, 2006, **242**, 217–226.

64 J. Xu and M. Saeys, *Chem. Eng. Sci.*, 2007, **62**, 5039–5041.

65 J. Xu and M. Saeys, *J. Phys. Chem. C*, 2009, **113**, 4099–4106.

66 A. Fouskas, M. Kollia, A. Kambolis, C. Papadopoulou and H. Matralis, *Appl. Catal., A*, 2014, **474**, 125–134.

67 K. F. Tan, J. Chang, A. Borgna and M. Saeys, *J. Catal.*, 2011, **280**, 50–59.

68 H.-X. Zhang, S.-H. Wang, K. Jiang, T. André and W.-B. Cai, *J. Power Sources*, 2012, **199**, 165–169.

69 K. Jiang, K. Xu, S. Zou and W. Bin Cai, *J. Am. Chem. Soc.*, 2014, **136**, 4861–4864.

70 J. S. Yoo, Z.-J. Zhao, J. K. Nørskov and F. Studt, *ACS Catal.*, 2015, **5**, 6579–6586.

71 T. Murata, K. Kotsuki, H. Murayama, R. Tsuji and Y. Morita, *Commun. Chem.*, 2019, **2**, 46.

72 T. T. Vo Doan, J. Wang, K. C. Poon, D. C. L. Tan, B. Khezri, R. D. Webster, H. Su and H. Sato, *Angew. Chem., Int. Ed.*, 2016, **55**, 6842–6847.

73 M. Wang, X. Qin, K. Jiang, Y. Dong, M. Shao and W. Bin Cai, *J. Phys. Chem. C*, 2017, **121**, 3416–3423.

74 J. Li, J. Chen, Q. Wang, W.-B. Cai and S. Chen, *Chem. Mater.*, 2017, **29**, 10060–10067.

75 L. Chen, L. Lu, H. Zhu, Y. Chen, Y. Huang, Y. Li and L. Wang, *Nat. Commun.*, 2017, **8**, 14136.

76 R. Jiang, D. T. Tran, J. P. McClure and D. Chu, *ACS Catal.*, 2014, **4**, 2577–2586.

77 H. Lv, L. Sun, D. Xu, J. Henzie, Y. Yamauchi and B. Liu, *J. Mater. Chem. A*, 2019, **7**, 24877–24883.

78 L. Sun, H. Lv, Y. Wang, D. Xu and B. Liu, *J. Phys. Chem. Lett.*, 2020, **11**, 6632–6639.

79 M. Crespo-Quesada, A. Yarulin, M. Jin, Y. Xia and L. Kiwi-Minsker, *J. Am. Chem. Soc.*, 2011, **133**, 12787–12794.

80 M.-K. Kang and J. Nielsen, *J. Ind. Microbiol. Biotechnol.*, 2017, **44**, 613–622.

81 A. Borodziński and G. C. Bond, *Catal. Rev.*, 2006, **48**, 91–144.

82 D. Teschner, J. Borsodi, A. Wootsch, Z. Revay, M. Havecker, A. Knop-Gericke, S. D. Jackson and R. Schlogl, *Science*, 2008, **320**, 86–89.

83 M. Inagaki, M. Toyoda, Y. Soneda and T. Morishita, *Carbon*, 2018, **132**, 104–140.

84 Y. Zhong, X. Xia, F. Shi, J. Zhan, J. Tu and H. J. Fan, *Adv. Sci.*, 2016, **3**, 1500286.

85 J. C. Crowhurst, A. F. Goncharov, B. Sadigh, J. M. Zaug, D. Aberg, Y. Meng and V. B. Prakapenka, *J. Mater. Res.*, 2008, **23**, 1–5.

86 V. A. de la Peña O'Shea, P. R. de la Piscina, N. Homs, G. Aromí and J. L. G. Fierro, *Chem. Mater.*, 2009, **21**, 5637–5643.

87 R. Lizárraga, F. Pan, L. Bergqvist, E. Holmström, Z. Gercsi and L. Vitos, *Sci. Rep.*, 2017, **7**, 3778.

88 O. Kitakami, H. Sato, Y. Shimada, F. Sato and M. Tanaka, *Phys. Rev. B: Condens. Matter Mater. Phys.*, 1997, **56**, 13849–13854.

89 P. van Helden, I. M. Ciobîcă and R. L. J. Coetzer, *Catal. Today*, 2016, **261**, 48–59.

90 L. Wang, W. Zhang, X. Zheng, Y. Chen, W. Wu, J. Qiu, X. Zhao, X. Zhao, Y. Dai and J. Zeng, *Nat. Energy*, 2017, **2**, 869–876.

91 R. Razzaq, C. Li, M. Usman, K. Suzuki and S. Zhang, *Chem. Eng. J.*, 2015, **262**, 1090–1098.

92 L. An, W. Huang, N. Zhang, X. Chen and D. Xia, *J. Mater. Chem. A*, 2014, **2**, 62–65.

93 H. Abroshan, P. Bothra, S. Back, A. Kulkarni, J. K. Nørskov and S. Siahrostami, *J. Phys. Chem. C*, 2018, **122**, 4783–4791.

94 Y. Yao, X. Lin and X. Zhang, *J. Mater. Sci.*, 2018, **53**, 7691–7702.

95 Y. Zhang, B. Ouyang, J. Xu, G. Jia, S. Chen, R. S. Rawat and H. J. Fan, *Angew. Chem., Int. Ed.*, 2016, **55**, 8670–8674.

96 Y. Zhou, Z. Zhou, R. Shen, R. Ma, Q. Liu, G. Cao and J. Wang, *Energy Storage Mater.*, 2018, **13**, 189–198.

97 Z. Rong, C. Dong, S. Zhang, W. Dong and F. Huang, *Nanoscale*, 2020, **12**, 6089–6095.

98 M. Jiang, C. Fu, R. Cheng, W. Zhang, T. Liu, R. Wang, J. Zhang and B. Sun, *Adv. Sci.*, 2020, **7**, 2000747.

99 Z. Chen, Y. Ha, Y. Liu, H. Wang, H. Yang, H. Xu, Y. Li and R. Wu, *ACS Appl. Mater. Interfaces*, 2018, **10**, 7134–7144.

100 H. Yin, C. Zhang, F. Liu and Y. Hou, *Adv. Funct. Mater.*, 2014, **24**, 2930–2937.

101 J. Suntivich, K. J. May, H. A. Gasteiger, J. B. Goodenough and Y. Shao-Horn, *Science*, 2011, **334**, 1383–1385.

102 C. Guan, A. Sumboja, W. Zang, Y. Qian, H. Zhang, X. Liu, Z. Liu, D. Zhao, S. J. Pennycook and J. Wang, *Energy Storage Mater.*, 2019, **16**, 243–250.

103 R. Xu, F. Luo, M. Li and Z. Yang, *Chem. Commun.*, 2019, **55**, 13394–13397.

104 Y. Niu, X. Huang, Y. Wang, M. Xu, J. Chen, S. Xu, M. Willinger, W. Zhang, M. Wei and B. Zhang, *Nat. Commun.*, 2020, **11**, 1–9.

105 M. Bauer, R. Schoch, L. Shao, B. Zhang, A. Knop-Gericke, M. Willinger, R. Schlögl and D. Teschner, *J. Phys. Chem. C*, 2012, **116**, 22375–22385.

106 R. Guo, Q. Chen, X. Li, Y. Liu, C. Wang, W. Bi, C. Zhao, Y. Guo and M. Jin, *J. Mater. Chem. A*, 2019, **7**, 4714–4720.

107 Q. Lai, T. Wang, Y. Sun and K.-F. Aguey-Zinsou, *Adv. Mater. Technol.*, 2018, **3**, 1700298.

108 A. J. Maeland and T. R. P. Gibb, *J. Phys. Chem.*, 1961, **65**, 1270–1272.

109 B. D. Adams and A. Chen, *Mater. Today*, 2011, **14**, 282–289.

110 Y. Fukai, *The Metal-Hydrogen System*, Springer, Berlin, Heidelberg, 1993, vol. 21.

111 D. E. Nanu, W. J. Legerstee, S. W. H. Eijt, W. G. Haije, J. F. Vente, M. G. Tucker and A. J. Böttger, *Acta Mater.*, 2008, **56**, 6132–6140.

112 J. Wang, L. Yu, L. Hu, G. Chen, H. Xin and X. Feng, *Nat. Commun.*, 2018, **9**, 1795.

113 Z. Zhao, X. Huang, M. Li, G. Wang, C. Lee, E. Zhu, X. Duan and Y. Huang, *J. Am. Chem. Soc.*, 2015, **137**, 15672–15675.

114 D. Gao, H. Zhou, F. Cai, D. Wang, Y. Hu, B. Jiang, W.-B. Cai, X. Chen, R. Si, F. Yang, S. Miao, J. Wang, G. Wang and X. Bao, *Nano Res.*, 2017, **10**, 2181–2191.

115 M. K. Kabiraz, J. Kim, W. J. Lee, B. Ruqia, H. C. Kim, S. U. Lee, J. R. Kim, S. M. Paek, J. W. Hong and S. Il Choi, *Chem. Mater.*, 2019, **31**, 5663–5673.

116 X.-T. Li, L. Chen, G.-F. Wei, C. Shang and Z.-P. Liu, *ACS Catal.*, 2020, **10**, 9694–9705.

117 J. Zhang, M. Chen, H. Li, Y. Li, J. Ye, Z. Cao, M. Fang, Q. Kuang, J. Zheng and Z. Xie, *Nano Energy*, 2018, **44**, 127–134.

118 W. Xu, G. Fan, J. Chen, J. Li, L. Zhang, S. Zhu, X. Su, F. Cheng and J. Chen, *Angew. Chem.*, 2020, **132**, 3539–3544.

119 Y. Lu, J. Wang, Y. Peng, A. Fisher and X. Wang, *Adv. Energy Mater.*, 2017, **7**, 1700919.

120 S. Wang, D. Tian, X. Wang, J. Qin, Y. Tang, J. Zhu, Y. Cong, H. Liu, Y. Lv, C. Qiu, Z. Gao and Y. Song, *Electrochem. Commun.*, 2019, **102**, 67–71.

121 L. Yan, X.-X. Liu and Y. Fu, *RSC Adv.*, 2016, **6**, 109702–109705.

122 B. L. Farrell, V. O. Igenegbai and S. Linic, *ACS Catal.*, 2016, **6**, 4340–4346.

123 T. Xie and R. M. Rioux, *Catal. Today*, DOI: 10.1016/j.cattod.2020.07.062.

124 I. T. Ellis, E. H. Wolf, G. Jones, B. Lo, M. Meng-Jung Li, A. P. E. York and S. C. Edman Tsang, *Chem. Commun.*, 2017, **53**, 601–604.

125 D. E. Brown, T. Edmonds, R. W. Joyner, J. J. McCarroll and S. R. Tennison, *Catal. Lett.*, 2014, **144**, 545–552.

126 J. Zheng, F. Liao, S. Wu, G. Jones, T. Chen, J. Fellowes, T. Sudmeier, I. J. McPherson, I. Wilkinson and S. C. E. Tsang, *Angew. Chem., Int. Ed.*, 2019, **58**, 17335–17341.

127 Y. Toda, H. Yanagi, E. Ikenaga, J. J. Kim, M. Kobata, S. Ueda, T. Kamiya, M. Hirano, K. Kobayashi and H. Hosono, *Adv. Mater.*, 2007, **19**, 3564–3569.

128 A. D. Pelton, *Bull. Alloy Phase Diagrams*, 1986, **7**, 223–228.

129 C. Autthanit, W. Chatkaew, P. Praserthdam and B. Jongsomjit, *J. Environ. Chem. Eng.*, 2020, **8**, 103547.

130 C. Krutpijit, W. Tian, B. Jongsomjit, D. Pjontek and J. E. Herrera, *Mol. Catal.*, 2020, **483**, 110717.